Monthly Notices of the ROYAL ASTRONOMICAL SOCIETY

MNRAS **528,** 4702–4719 (2024) https://doi.org/10.1093/mnras/stae310
Advance Access publication 2024 February 2

Detection of an intranight optical hard lag with colour variability in blazar PKS 0735+178

Callum McCall [1]★ Helen E. Jermak,[1] Iain A. Steele,[1] Shiho Kobayashi,[1] Johan H. Knapen[2,3] and Pablo M. Sánchez-Alarcón[2,3]

[1]*Astrophysics Research Institute, Liverpool John Moores University, Liverpool Science Park IC2, 146 Brownlow Hill, Liverpool, UK, L3 5RF*
[2]*Instituto de Astrofísica de Canarias, c/Vía Láctea s/n, E-38205 La Laguna, Tenerife, Spain*
[3]*Departamento de Astrofísica, Universidad de La Laguna, E-38206 La Laguna, Tenerife, Spain*

Accepted 2024 January 26. Received 2023 December 20; in original form 2023 November 10

ABSTRACT

Blazars are a highly variable subclass of active galactic nuclei that have been observed to vary significantly during a single night. This intranight variability remains a debated phenomenon, with various mechanisms proposed to explain the behaviour including jet energy density evolution or system geometric changes. We present the results of an intranight optical monitoring campaign of four blazars: TXS 0506+056, OJ287, PKS 0735+178, and OJ248 using the Carlos Sánchez Telescope. We detect significant but colourless behaviour in OJ287 and both bluer- and redder-when-brighter colour trends in PKS 0735+178. Additionally, the g band shows a lag of ~ 10 min with respect to the r, i, z_s bands for PKS 0735+178 on 2023 January 17. This unexpected hard lag in PKS 0735+178 is not in accordance with the standard synchrotron shock cooling model (which would predict a soft lag) and instead suggests the variability may be a result of changes in the jet's electron energy density distribution, with energy injection from Fermi acceleration processes into a post-shocked medium.

Key words: galaxies: active – BL Lacertae objects: TXS 0506+056 – BL Lacertae objects: OJ287 – BL Lacertae objects: PKS 0735+178 – galaxies: jets – quasars: OJ248.

1 INTRODUCTION

At the centre of most galaxies resides a supermassive black hole (SMBH) and if subject to accretion, this SMBH can be referred to as an active galactic nucleus (AGN). A blazar is an AGN where the relativistic jet emanating from the polar regions of the black hole is oriented along our line of sight within $\lesssim 15^\circ$ (Hovatta et al. 2009). The resulting relativistic beaming produces highly variable emission across the electromagnetic spectrum (Urry 1998).

Blazars can be categorized into two classes based on the features within their optical spectra. BL Lac-types have near featureless optical spectra, whereas flat spectrum radio quasars (FSRQs) show emission lines with EW $\geq$5 Å (Stickel et al. 1991). The spectral energy distribution of blazars has a distinct double-hump structure with a lower-energy peak at IR to X-ray frequencies and a higher-energy peak at X-ray to HE γ-rays (Fossati et al. 1998). The lower-energy peak is attributed to synchrotron emission from the jet, whereas the source of the higher-energy peak is still debated (Ghisellini et al. 1998; Prandini & Ghisellini 2022). This second peak can be explained through leptonic models, where the emission is attributed to lower-energy seed photons being up-scattered by relativistic electrons through inverse-Compton scattering (Böttcher et al. 2013). The source of these seed photons can be from within (synchrotron self-Compton; Maraschi, Ghisellini & Celotti 1992) or from outside (external Compton; Dermer & Schlickeiser 1993) the jet. This means relationships between the lower- and higher-energy regimes are likely, as their origin is the same population of electrons. Conversely, hadronic models involving interactions between protons and/or mesons might explain the high-energy variability independently of the lower-energy emission (Böttcher et al. 2013). These hadronic models are also important for the production of HE neutrinos (Osorio et al. 2023).

The location of the lower-energy peak can be used to distinguish between different blazar classes and BL Lac-type subclasses. Low synchrotron peaked (LSP) sources have a synchrotron peak $< 10^{14}$ Hz, corresponding to IR emission, and can be FSRQs or BL Lacs (low-frequency peaked BL Lacs; LBLs). Only BL Lacs have synchrotron peaks at higher frequencies. High synchrotron peaked (HSP or high-frequency peaked BL Lacs; HBLs) sources have synchrotron peaks $>10^{15}$ Hz in UV or X-ray; those with a synchrotron peak frequency in the optical regime between 10^{14} Hz $\leq \nu \leq 10^{15}$ Hz are classed as intermediate synchrotron peaked (ISP) sources or intermediate-frequency peaked BL Lacs (IBLs; Urry & Padovani 1995; Abdo et al. 2010).

Blazars can show variability on a variety of time-scales, from years down to minutes, with the latter being referred to as intranight variability. The intranight optical variability (INOV) of blazars has been the focus of numerous campaigns over the past 30 yr (Miller, Carini & Goodrich 1989; Sagar et al. 2004; Chand et al. 2021), but it is still not a well-understood characteristic of their emission. There have been many models proposed to explain the different types of

★ E-mail: callumlmccall@gmail.com

variability such as quasi-periodic oscillations (QPOs; Jorstad et al. 2022), micro-flares (Bhatta et al. 2015), and gradual flux changes (Subbu Ulaganatha Pandian et al. 2022), observed over hour-long time-scales. These models can predict time lags between different wavebands, colour evolution, and polarization degree and angle changes. Such models include geometric changes related to the jet angle and Doppler factors of emitting blobs (Gopal-Krishna & Wiita 1992), intrinsic changes relating to particle energy distributions (Bachev et al. 2012; Bachev 2015), and extrinsic changes including microlensing from objects outside the blazar system along our line of sight (Paczynski 1996).

Colour evolution in blazars generally takes one of two forms: bluer-when-brighter (BWB) or redder-when-brighter (RWB). In general, BL Lac-type sources tend to exhibit BWB trends and where this is not the case and an RWB trend is seen, the objects tend to be host-galaxy-dominated (Negi et al. 2022). FSRQs can be found showing both BWB and RWB trends, but the proportion of sources that exhibit the latter is much greater than among BL Lacs (Zhang et al. 2015; Negi et al. 2022). In any case, the colour changes of blazars can be used to determine the origin of the emission and refine emission mechanisms. The BWB chromatism may arise from a number of different mechanisms. One proposed mechanism is synchrotron cooling of internal shock accelerated electrons, where higher-energy electrons cool faster making bluer light appear more variable than redder light (Kirk, Rieger & Mastichiadis 1998). Another is the one-component synchrotron model where an increase in the energy output of the blazar increases the average particle energy and thus the frequency, making the blazar appear BWB (Fiorucci, Ciprini & Tosti 2004). When in faint states or periods of jet quiescence, redder emission and variability from the accretion disc may become visible leading to RWB behaviour; this is true for both BL Lac- and FSRQ-type blazars. A potential explanation of why more FSRQs show general RWB behaviour may come from the flattening of their spectral slope at optical frequencies from the presence of the 'UV bump'. The RWB behaviour, or steepening of the composite thermal and non-thermal spectrum, could be explained if the non-thermal component had a greater contribution towards the total flux during brightening (Gu et al. 2006).

Similarly to colour variability, time lags (or a lack thereof) can help constrain emission processes. Time lags between different frequencies have been observed in numerous studies (Chatterjee et al. 2008; Gaur, Gupta & Wiita 2012; Liodakis et al. 2018), but inter-band lags within the optical waveband are much less commonly observed, with the first proposed detection in 2009 (Wu et al. 2009). The internal shock model (Kirk et al. 1998) predicts time lags across all synchrotron emission frequencies and therefore within the optical waveband. The rate of synchrotron cooling is frequency dependent, meaning variability at higher energy precedes that at lower energies (Kirk et al. 1998).

INOV including colour evolution and inter-band time lags is difficult to detect for a number of reasons, both physical to the system and logistically in terms of observational cadence, and can result in data with irregular or limited time resolution (Böttcher & Dermer 2010).

In this paper, we present the results of a five-night INOV monitoring campaign executed over the period 2023 January 15–19 on four blazars: TXS 0506+056, OJ287, PKS 0735+178, and OJ248. These sources were chosen due to a combination of their historic degrees of INOV and their observability during the campaign. The sample was kept small to ensure the data were sufficient to observe hour-long variability time-scales with high sampling.

In Section 2, we describe the facilities and instruments used and photometric analysis procedures including statistical processes. In Section 3, we describe the individual sources and their historical behaviour. In Sections 4–6, we present the results of the correlation analyses including variability indicators, colour behaviour, and time lags. In Section 7, we discuss the implication of the results from the analysis.

2 OBSERVATIONS AND DATA REDUCTION

2.1 Carlos Sánchez Telescope – MuSCAT2

Observations were taken with the four-colour simultaneous imager MuSCAT2 (Narita et al. 2019) located on the 1.52 m Carlos Sánchez Telescope (TCS) at the Teide Observatory, Tenerife. The TCS has a Dall-Kirkham configuration with a focal length of *f*/13.8 and the MuSCAT2 instrument is fixed at the Cassegrain focus. MuSCAT2 achieves four-colour simultaneous observations through the use of three dichroic mirrors to separate the light into four wavelength bands [g (400–550nm), r (550–700nm), i (700–820nm), z_s (820–920nm) where the subscript 's' here denotes the 'shorter' waveband range to a traditional z band filter] to be detected by four fast-readout PIXIS CCD cameras. The derived pixel scales of ~ 0.44 arcsec pixel^{-1} across each band correspond to a field of view (FOV) of 7.4×7.4 arcsec^2 in all filters (Narita et al. 2019).

A summary of the TCS observations is presented in Table 1. Each source was observed on three separate nights and, in general, observations were interleaved for two sources with a typical observing sequence of 10 frames per source with a 30-s exposure time (the longest that could be executed without autoguiding; imposed by an autoguider failure).

2.2 Liverpool Telescope – MOPTOP

Supplementary observations were carried out with the MOPTOP (Shrestha et al. 2020) polarimeter on the fully robotic 2 m Liverpool Telescope (LT) located at the Observatorio del Roque de los Muchachos, La Palma. The LT has a Ritchey-Chrétien Cassegrain design with MOPTOP fitted at one of the science fold ports.

MOPTOP boasts a dual-beam configuration utilizing a continuously rotating half-wave plate and two fast readout very low noise CMOS cameras. Together, these allow MOPTOP to achieve high sensitivity and time resolution while minimizing systematic errors. MOPTOP has a 7×7 arcsec^2 FOV (Shrestha et al. 2020). The data were taken in B (380–520 nm), V (490–570 nm), and R (580–695 nm) filters quasi-simultaneously (observations with different filters taken in succession).

The observations with MOPTOP were taken much less frequently than those of MuSCAT2, aiming for a few observations each night wherever possible. Observations were taken on 2023 January 15–16 before poor weather conditions in La Palma closed the observatory for the remainder of the campaign.

2.3 Data reduction

The data were calibrated and analysed using the ASTROPY Python package and standard differential photometry techniques. MuSCAT2 frames required bias/dark subtraction and flat fielding and this was performed using calibration frames taken before/after observations each night. The data also required a WCS fit which was performed using the ASTROMETRY.NET API (Lang et al. 2010). MOPTOP reduction is carried out using an automated data reduction pipeline

Table 1. List of the blazars used in this analysis including the source right ascension (α), declination (δ), type, redshift (z), TCS observation date, hours observed (H), and the number of observations (N) in g, r, i, z_s bands.

Name	α (J2000)	δ (J2000)	Type	z	Date	H	N
TXS 0506+056	$05^h09^m25\overset{s}{.}96$	$+05°41'35\overset{''}{.}333$	LSP	0.337	2023 Jan 15	5.15	121
...	...	...	...	...	2023 Jan 16	1.43	157
...	...	...	...	...	2023 Jan 18	0.87	100
OJ287	$08^h54^m48\overset{s}{.}875$	$+20°06'30\overset{''}{.}640$	LSP	0.306	2023 Jan 15	7.95	216
...	...	...	...	...	2023 Jan 18	2.62	294
...	...	...	...	...	2023 Jan 19	0.29	17
PKS 0735+178	$07^h38^m07\overset{s}{.}394$	$+17°42'18\overset{''}{.}998$	ISP	0.45	2023 Jan 15	3.22	77
...	...	...	...	...	2023 Jan 16	0.63	25
...	...	...	...	...	2023 Jan 17	7.24	313
OJ248	$08^h30^m52\overset{s}{.}086$	$+24°10'59\overset{''}{.}820$	FSRQ	0.939	2023 Jan 16	0.61	29
...	...	...	...	...	2023 Jan 17	7.33	250
...	...	...	...	...	2023 Jan 19	0.74	66

running at the telescope which provides bias/dark subtracted, flat-fielded, and WCS-fitted frames (Smith et al. 2016).

The MuSCAT2 photometric data were calibrated by calculating the weighted average zero point in each frame using estimates from five in-frame calibration stars with known $griz_s$ magnitudes from SDSS, Pan-STARRS, and APASS catalogues (Henden et al. 2018; Flewelling et al. 2020; Abdurro'uf et al. 2022). This zero point was then used to calibrate the data for the source.

MOPTOP photometric data were calibrated using an in-frame reference star with known *BVR* magnitudes. Polarimetric data were calibrated using observations of zero-polarized standard stars to calculate instrumental polarization values (q_0 and u_0) and polarized standard stars to find the instrumental position angle values.

Before applying statistical methods and generating light curves, the data were sigma-clipped using the Python package ASTROPY as a form of quality control. In this process, data are removed if they are above or below three times the standard deviation from the median value. This is an iterative process that produces updated median and standard deviation values until no further values are removed. Applying this to the flux values at each epoch, disproportionate variability between filters caused by erroneous pixels or poor sky conditions was removed. The final amount of data removed equates to less than 10 per cent (and in most cases less than 5 per cent) per source per epoch.

We note that no correction for host galaxy contribution to the source magnitudes or colours has been applied. In general, blazars of subclasses LSP and ISP outshine their host galaxies by several orders of magnitude, so significant host galaxy emission is only observed when the AGN is in a very low state in combination with deep photometric imaging (Nilsson et al. 2012; Gaur 2014; Olguín-Iglesias et al. 2016). None of our sources were in such a state.

3 TARGETS

3.1 TXS 0506+056

TXS 0506+056 is situated at a redshift of 0.337 (Paiano et al. 2018) and until recently was classified as an LSP BL Lac (LBL) object (Fan et al. 2014). It has been proposed that TXS 0506+056 may belong to a subclass of blazars named masquerading BL Lacs, or blue FSRQs (Ghisellini et al. 2012; Padovani et al. 2019; Lewis et al. 2021), where the Doppler-boosted synchrotron radiation in the relativistic jet is bright enough to outshine the broad line region (Rodrigues et al. 2019; Rajagopal et al. 2020). This would make the FSRQ appear as a BL Lac object due to the apparent lack of emission lines.

In 2017 September, TXS 0506+056 was found to be in a consistent location with the IceCube neutrino event EHE 170922A (Kopper & Blaufuss 2017) to within a 3σ significance level (IceCube Collaboration et al. 2018) while in a state of heightened γ-ray activity (Tanaka, Buson & Kocevski 2017). Since then, the object has been the subject of various studies over different frequencies and time-scales (see Keivani et al. 2018; Bachev et al. 2021; Acciari et al. 2022).

We observed TXS 0506+056 over three nights, totalling 7.45 h in the $griz_s$ filters. We obtained complementary photo-polarimetric data with MOPTOP on the LT in the *BVR* bands to assess the polarimetric state of the source during the observing campaign. We also took *Fermi* γ-ray data from the Light Curve Repository (LCR; Abdollahi et al. 2023). The *Fermi* data showed TXS 0506+056 to be in a γ-ray state a little higher than its median flux level over all time, at $6.63 \pm 6.05 \times 10^{-8}$ 0.1–100 GeV ph cm^{-2} s^{-1} (median level: $8.30 \pm 0.23 \times 10^{-8}$ 0.1–100 GeV ph cm^{-2} s^{-1}). Its optical linear polarization degree varied between roughly 9 and 16 per cent and the polarization angle varied between approximately 150° and 170° across all *BVR* bands.

3.2 OJ287

OJ287 is located at a redshift of 0.306 (Sitko & Junkkarinen 1985) and is a well-known LBL (Nilsson et al. 2018). OJ287 is one of the best binary SMBH candidates with a double-peaked outburst period of roughly 12 yr (Sillanpaa et al. 1988, 1996). The observed optical outbursts date back over 130 yr, corresponding to the interaction of the secondary black hole with the primary's accretion disc. A second, longer period of approximately 60 yr has also been reported (Valtonen et al. 2006) which is thought to arise from the orbital precession inducing a precession into the accretion disc (Katz 1997; Sundelius et al. 1997) and causing a subsequent wobble in the jet angle.

We observed OJ287 over three nights, totalling 10.86 h in the $griz_s$ filters. Additional MOPTOP photo-polarimetric data showed the optical linear polarization degree varied between roughly 10 and 25 per cent and its polarization angle varied between approximately 160° and 175° across all *BVR* bands. *Fermi* γ-ray data from the LCR (Abdollahi et al. 2023) showed OJ287 to be in a γ-ray state a little lower than its median flux level over all time, at $3.77 \pm 2.93 \times 10^{-8}$ 0.1–100 GeV ph cm^{-2} s^{-1} (median level: $5.94 \pm 0.31 \times 10^{-8}$ 0.1–100 GeV ph cm^{-2} s^{-1}).

3.3 PKS 0735+178

PKS 0735+178 is an ISP BL Lac-type object with a disputed redshift as a result of its featureless optical spectrum. A lower limit of $z \geq 0.424$ was first proposed by Carswell et al. (1974) after the detection of a strong absorption feature, and has since been refined using the detection of the host galaxy using deep *I* band imaging when the central engine was in a faint state ($z = 0.45 \pm 0.06$; Nilsson et al. 2012), and the surrounding galaxies ($z \sim 0.65$; Stickel, Fried & Kuehr 1993; Falomo, Treves & Paiano 2021). Sahakyan et al. (2023) compare the multiwavelength data to that of TXS 0506+056, another blazar neutrino candidate, and utilize conditions set out in Padovani et al. (2019) to conclude that like TXS 0506+056, PKS 0735+178 may also be a masquerading BL Lac as a result of a radio power $P_{1.4\,\mathrm{GHz}} > 10^{26}\,\mathrm{W\,Hz^{-1}}$ and a γ-ray Eddington ratio $L_\gamma/L_{\mathrm{Edd}} \gtrsim 0.1$.

In 2021 December, PKS 0735+178 underwent its largest ever recorded flaring event across radio (Kadler et al. 2021), optical (Zhirkov et al. 2021), X-ray (Santander & Buson 2021), and γ-ray (Garrappa et al. 2021) frequencies while being in spacial coincidence with neutrino events reported by IceCube Collaboration (2021), Dzhilkibaev, Suvorova & Baikal-GVD Collaboration (2021), Petkov et al. (2021), and Filippini et al. (2022).

We observed PKS 0735+178 over three nights, totalling 11.09 h in the $griz_s$ filters. Its *Fermi* data (from the LCR; Abdollahi et al. 2023) showed PKS 0735+178 to be in a γ-ray state higher than its median flux level over all time, at $4.41 \pm 0.71 \times 10^{-7}$ 0.1–100 GeV ph cm^{-2} s^{-1} (median level: $5.69 \pm 0.35 \times 10^{-8}$ 0.1–100 GeV ph cm^{-2} s^{-1}). Its polarimetric properties were measured with MOPTOP, and showed its optical linear polarization degree decreased from roughly 8 to 3 per cent and polarization angle increased from approximately 80° to 120° across all *BVR* bands.

3.4 OJ248

OJ248 is an FRSQ at redshift $z \sim 0.939$ (Massaro et al. 2015). A long-term multiwavelength analysis of this source was performed by the GASP-WEBT Collaboration from 2006–2013 (Carnerero et al. 2015) including data at radio, NIR, optical, X-ray, and γ-ray frequencies. A large multiwavelength flare was observed in late 2012 by WEBT, *Swift* (D'Ammando & Orienti 2012), and *Fermi* (Orienti & D'Ammando 2012) as well as an additional radio outburst in late 2010 and optical-NIR flare in early 2007.

We observed OJ248 over three nights, totalling 8.68 h in the $griz_s$ filters. Its optical polarization degree, measured by MOPTOP, was below 5 per cent in *V* band. *Fermi* γ-ray data from the LCR (Abdollahi et al. 2023) showed OJ248 to be in a γ-ray state consistent with its median flux level over all time, at $7.02 \pm 5.44 \times 10^{-8}$ 0.1–100 GeV ph cm^{-2} s^{-1} (median level: $8.22 \pm 0.88 \times 10^{-8}$ 0.1–100 GeV ph cm^{-2} s^{-1}).

4 TEMPORAL VARIABILITY

The $griz_s$ light curves for each source on a given night are shown in Figs B1–B4 for TXS 0506+056, OJ287, PKS 0735+178, and OJ248, respectively. The source name and night of observation are given above each plot.

In order to quantify variability in the light curves and to disentangle intrinsic variability from noise, we employ several statistical tests to determine the variability likelihood. Specifically, we calculate the variability amplitude and fractional variability and perform chi-squared and enhanced *F*-test analyses. These tests are detailed in Sections 4.1–4.4.

4.1 Variability amplitude

Variability amplitude is defined in Heidt & Wagner (1996) as

$$\mathrm{VA} = \sqrt{(x_{\max} - x_{\min})^2 - 2\langle x_{\mathrm{err}}\rangle^2}, \tag{1}$$

where $x_{\max}$ and $x_{\min}$ are the maximum and minimum observed values, and $\langle x_{\mathrm{err}}\rangle$ is the median measurement error. The percentage variability amplitude, $\mathrm{VA_{per}}$, is given in Romero, Cellone & Combi (1999) as

$$\mathrm{VA_{per}} = \frac{100}{\langle x\rangle}\sqrt{(x_{\max} - x_{\min})^2 - 2\langle x_{\mathrm{err}}\rangle^2}, \tag{2}$$

where $\langle x\rangle$ is the average observed value. Its error, $\Delta\mathrm{VA_{per}}$, is given in Singh et al. (2018) as

$$\Delta\mathrm{VA_{per}} = 100 \times \left(\frac{x_{\max} - x_{\min}}{\langle x\rangle \times \mathrm{VA}}\right) \times \sqrt{\left(\frac{x_{\mathrm{err,max}}}{\langle x\rangle}\right)^2 + \left(\frac{x_{\mathrm{err,min}}}{\langle x\rangle}\right)^2 + \left(\frac{\langle x_{\mathrm{err}}\rangle}{x_{\max} - x_{\min}}\right)^2 \mathrm{VA}^4}, \tag{3}$$

where $x_{\mathrm{err,max}}$ and $x_{\mathrm{err,min}}$ are the errors on the maximum and minimum values, respectively. The variability amplitude aims to provide a quantification of the absolute range of variability of a given source by simply looking at the range of magnitudes outside of the scatter from the measurement errors.

The values obtained via the variability amplitude calculations can be seen in column 4 in Table 2. We find variability amplitudes ranging from 0.167 per cent up to 1.456 per cent across all sources, dates, and filters. The ratio between the error and percentage variability amplitude shows that in 12/48 cases the percentage variability amplitudes are associated with large errors (where the ratio is greater than 3). We note that nine of these cases are attributed to the source OJ248; likely due to it being the faintest of the sample.

4.2 Fractional variability

Fractional variability, described fully in Schleicher et al. (2019), is a method of quantifying variability intensity while accounting for measurement uncertainties. It differs from the variability amplitude by considering the variability relative to the mean brightness level. It is defined in Edelson et al. (2002) as

$$F_{\mathrm{var}} = \sqrt{\sigma^2_{\mathrm{NXS}}} = \sqrt{\frac{S^2 - \langle\sigma^2_{\mathrm{err}}\rangle}{\langle x\rangle^2}}, \tag{4}$$

where S^2 is the variance of the data set, $\langle\sigma^2_{\mathrm{err}}\rangle$ is the median square error, and $\langle x\rangle$ is the median value. It can also be given as the square root of the normalized excess variance (σ^2_{NXS}). Its associated error is given in Poutanen, Zdziarski & Ibragimov (2008) as

$$\Delta F_{\mathrm{var}} = \sqrt{\mathrm{F^2_{var}} + \Delta\sigma^2_{\mathrm{NXS}}} - F_{\mathrm{var}}, \tag{5}$$

where $\Delta\sigma^2_{\mathrm{NXS}}$ is the error on the normalized excess variance. This error is given in Vaughan et al. (2003) as

$$\Delta\sigma^2_{\mathrm{NXS}} = \sqrt{\left(\sqrt{\frac{2}{N}}\frac{\langle\sigma^2_{\mathrm{err}}\rangle}{\langle x\rangle^2}\right) + \left(\sqrt{\frac{\langle\sigma^2_{\mathrm{err}}\rangle}{N}}\frac{2F_{\mathrm{var}}}{\langle x\rangle}\right)^2}, \tag{6}$$

where N is the number of data points in the sample. It follows that if the variance is less than the average square error, $S^2 < \langle\sigma^2_{\mathrm{err}}\rangle$, a real value cannot be computed and will be denoted as <0, indicating

Table 2. Variability analysis results. From left to right: the source name, date of observation, and filter is given. VA represents the variability amplitude with error as described in Section 4.1, $F_{\rm var}$ is the fractional variability with error as described in Section 4.2, χ^2 is the Chi-squared value given with the critical value as described in Section 4.3, and $F_{\rm enh}$ is the enhanced F-test value with the critical value as described in Section 4.4. The final column describes whether or not the source was deemed variable in a particular filter on a given night. Of the three variability tests ($F_{\rm var}$, χ^2, and $F_{\rm enh}$), if all three showed variability the source was deemed variable (V), two meant possibly variable (PV), and one or none meant likely not variable (NV).

Source	Date	Filter	VA $\pm$ ΔVA(%)	$F_{\rm var} \pm \Delta F_{\rm var}$	$\chi^2(\chi^2_{\rm crit})$	$F_{\rm enh}(F_{\rm crit})$	Variable?
TXS 0506+056	230115	g	0.311 $\pm$ 0.003	0.04 $\pm$ 0.10	487.23 (181.99)	0.67 (1.54)	NV
...	...	r	0.368 $\pm$ 0.004	0.05 $\pm$ 0.11	420.57 (181.99)	0.91 (1.54)	NV
...	...	i	0.398 $\pm$ 0.003	0.05 $\pm$ 0.09	575.73 (181.99)	1.02 (1.54)	NV
...	...	$z_{\rm z}$	0.499 $\pm$ 0.006	0.06 $\pm$ 0.12	303.86 (181.99)	1.23 (1.54)	NV
TXS 0506+056	230116	g	0.225 $\pm$ 0.004	0.02 $\pm$ 0.30	195.04 (213.97)	1.17 (1.48)	NV
...	...	r	0.291 $\pm$ 0.005	0.02 $\pm$ 0.33	185.92 (213.97)	1.05 (1.48)	NV
...	...	i	0.258 $\pm$ 0.004	0.03 $\pm$ 0.20	255.78 (213.97)	1.48 (1.48)	PV
...	...	$z_{\rm z}$	0.294 $\pm$ 0.008	<0	138.42 (213.97)	1.13 (1.48)	NV
TXS 0506+056	230118	g	0.231 $\pm$ 0.004	0.03 $\pm$ 0.24	151.25 (147.01)	0.65 (1.63)	NV
...	...	r	0.183 $\pm$ 0.004	<0	87.88 (147.01)	0.93 (1.63)	NV
...	...	i	0.167 $\pm$ 0.004	0.01 $\pm$ 0.67	100.20 (147.01)	0.59 (1.63)	NV
...	...	$z_{\rm z}$	0.221 $\pm$ 0.006	<0	95.45 (147.01)	1.34 (1.63)	NV
OJ287	230115	g	0.615 $\pm$ 0.006	0.12 $\pm$ 0.06	1575.69 (281.37)	1.45 (1.40)	V
...	...	r	0.517 $\pm$ 0.005	0.09 $\pm$ 0.07	1212.16 (281.37)	1.74 (1.40)	V
...	...	i	0.628 $\pm$ 0.005	0.11 $\pm$ 0.05	2472.15 (281.37)	1.82 (1.40)	V
...	...	$z_{\rm z}$	0.679 $\pm$ 0.010	0.11 $\pm$ 0.08	962.74 (281.37)	1.59 (1.40)	V
OJ287	230118	g	0.539 $\pm$ 0.008	0.07 $\pm$ 0.13	569.87 (369.03)	0.94 (1.34)	NV
...	...	r	0.519 $\pm$ 0.009	0.06 $\pm$ 0.15	489.41 (369.03)	1.04 (1.34)	NV
...	...	i	0.503 $\pm$ 0.009	0.08 $\pm$ 0.10	796.89 (369.03)	1.23 (1.34)	NV
...	...	$z_{\rm z}$	0.534 $\pm$ 0.014	0.06 $\pm$ 0.16	445.58 (369.03)	0.86 (1.34)	NV
OJ287	230119	g	0.398 $\pm$ 0.015	0.06 $\pm$ 0.40	23.90 (42.31)	1.22 (3.07)	NV
...	...	r	0.497 $\pm$ 0.012	0.08 $\pm$ 0.29	25.79 (42.31)	0.66 (3.07)	NV
...	...	i	0.189 $\pm$ 0.007	<0	11.46 (42.31)	0.26 (3.07)	NV
...	...	$z_{\rm z}$	0.349 $\pm$ 0.018	<0	7.76 (42.31)	0.56 (3.07)	NV
PKS0735+178	230115	g	0.591 $\pm$ 0.004	0.12 $\pm$ 0.06	1194.61 (116.09)	6.17 (1.76)	V
...	...	r	0.427 $\pm$ 0.004	0.09 $\pm$ 0.08	564.00 (116.09)	4.01 (1.76)	V
...	...	i	0.509 $\pm$ 0.005	0.11 $\pm$ 0.06	833.54 (116.09)	5.54 (1.76)	V
...	...	$z_{\rm z}$	0.632 $\pm$ 0.010	0.13 $\pm$ 0.09	405.05 (116.09)	5.35 (1.76)	V
PKS0735+178	230116	g	0.415 $\pm$ 0.005	0.08 $\pm$ 0.13	138.44 (52.62)	5.63 (2.59)	PV
...	...	r	0.325 $\pm$ 0.005	0.06 $\pm$ 0.22	61.50 (52.62)	3.88 (2.59)	PV
...	...	i	0.447 $\pm$ 0.005	0.08 $\pm$ 0.14	109.87 (52.62)	6.12 (2.59)	PV
...	...	$z_{\rm z}$	0.353 $\pm$ 0.008	0.06 $\pm$ 0.28	46.23 (52.62)	2.45 (2.59)	NV
PKS0735+178	230117	g	0.992 $\pm$ 0.008	0.22 $\pm$ 0.03	6815.45 (383.68)	16.00 (1.33)	V
...	...	r	0.883 $\pm$ 0.009	0.22 $\pm$ 0.03	5214.03 (383.68)	21.84 (1.33)	V
...	...	i	0.825 $\pm$ 0.008	0.19 $\pm$ 0.04	4846.07 (383.68)	16.31 (1.33)	V
...	...	$z_{\rm z}$	0.769 $\pm$ 0.013	0.18 $\pm$ 0.07	1711.95 (383.68)	8.24 (1.33)	V
OJ248	230116	g	0.717 $\pm$ 0.020	0.08 $\pm$ 0.34	27.81 (56.89)	0.29 (2.46)	NV
...	...	r	0.588 $\pm$ 0.020	0.04 $\pm$ 0.89	27.86 (56.89)	0.31 (2.46)	NV
...	...	i	0.533 $\pm$ 0.027	<0	20.36 (56.89)	0.09 (2.46)	NV
...	...	$z_{\rm z}$	0.946 $\pm$ 0.062	<0	19.79 (56.89)	0.43 (2.46)	NV
OJ248	230117	g	0.746 $\pm$ 0.019	0.09 $\pm$ 0.19	398.02 (340.74)	0.28 (1.35)	NV
...	...	r	0.886 $\pm$ 0.027	0.07 $\pm$ 0.30	317.50 (340.74)	0.17 (1.35)	NV
...	...	i	1.193 $\pm$ 0.036	0.12 $\pm$ 0.20	405.82 (340.74)	0.20 (1.35)	NV
...	...	$z_{\rm z}$	1.456 $\pm$ 0.088	<0	192.61 (340.74)	0.22 (1.35)	NV
OJ248	230119	g	0.775 $\pm$ 0.021	0.11 $\pm$ 0.24	104.02 (107.26)	0.51 (1.81)	NV
...	...	r	0.967 $\pm$ 0.034	0.09 $\pm$ 0.41	77.57 (107.26)	0.36 (1.81)	NV
...	...	i	0.884 $\pm$ 0.033	0.07 $\pm$ 0.53	70.36 (107.26)	0.24 (1.81)	NV
...	...	$z_{\rm z}$	1.135 $\pm$ 0.067	<0	54.00 (107.26)	0.56 (1.81)	NV

detection of insignificant variability. Where sources had $F_{\rm var} > \Delta F_{\rm var}$, this test is deemed to show that an object has shown significant variability.

The fractional variability values are shown in column 5 in Table 2. We find 12/48 instances across all sources, dates, and filters where significant levels of variability have been detected. These detections correspond to OJ287 on 2023 January 15, and PKS 0735+178 on 2023 January 15 and 17 across all filters, with the most significant detections corresponding to PKS 0735+178 on 2023 January 17.

4.3 Chi-squared

Chi-squared (χ^2), as used in Zeng et al. (2017), is given by

$$\chi^2 = \sum_i^N \left(\frac{x_i - \langle x \rangle}{x_{{\rm err},i}} \right)^2 , \quad (7)$$

where x_i and $x_{{\rm err},i}$ are the individual values and errors respectively within the data set, and $\langle x \rangle$ is the median value. Its critical value was determined at the 99.9 per cent confidence level ($\alpha = 0.001$) with the

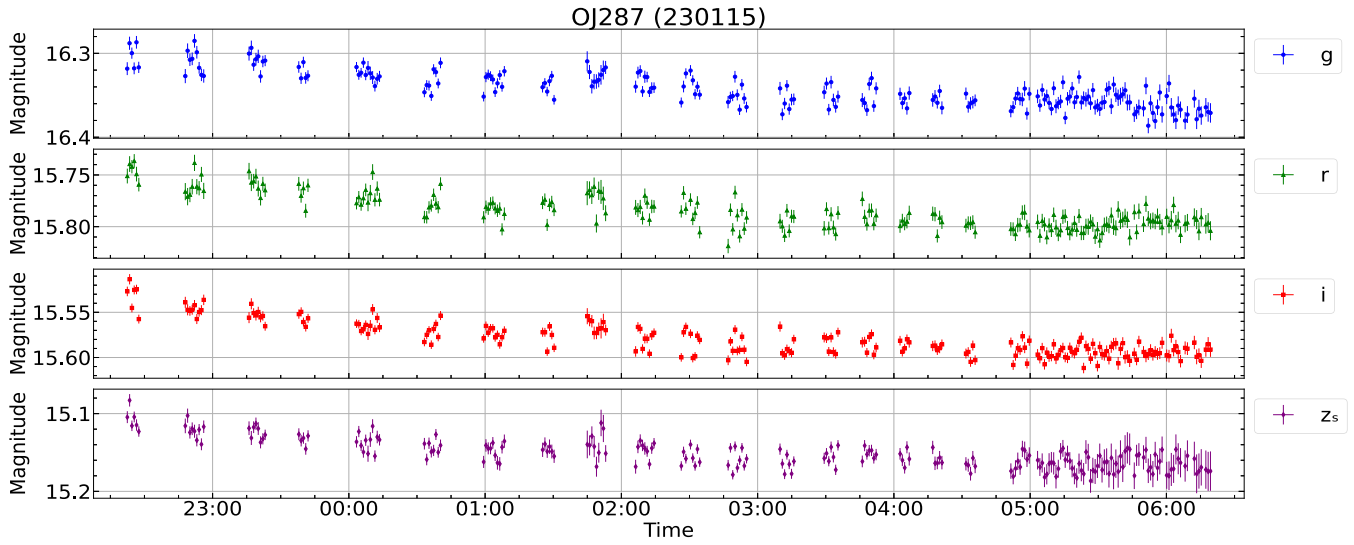

Figure 1. Light curves for OJ287 on the night of 2023 January 15. Panels correspond to g, r, i, z_s data separately, from top to bottom. Time is given in UTC.

degrees of freedom being equal to the number of data points. Where the value is greater than the critical value, significant variability has been detected. χ^2 is a useful metric as it quantifies the levels of variability about the median values. Incorporating the critical value allows us to determine the significance of the value.

The χ^2 values together with critical values are shown in column 6 in Table 2. With the χ^2 test, we detect significant variability in 27/48 instances across all sources, dates, and filters. In most cases, non-detection is consistent across filters per source per date. We find consistent variability detections across all filters for TXS 0506+056 on 2023 January 15, OJ287 on 2023 January 15 and 18, and PKS 0735+178 on 2023 January 15 and 17.

4.4 Enhanced *F*-test

The enhanced F-test ($F_{\rm enh}$) is given in de Diego (2014) and aims to quantify the variability of a target while incorporating the variability of multiple reference stars (Subbu Ulaganatha Pandian et al. 2022). It is given as

$$F_{\rm enh} = \frac{S^2_{\rm blazar}}{S^2_{\rm star}}, \tag{8}$$

where $S^2_{\rm blazar}$ is the variance of the blazar and $S^2_{\rm star}$ is the combined variance of the comparison stars. $S^2_{\rm star}$ is defined as

$$S^2_{\rm star} = \frac{1}{(\sum_{j=1}^{k} N_j - k)} \sum_{j=1}^{k} \sum_{i=1}^{N_j} \sigma_{j,i}, \tag{9}$$

where N_j is the number of observations of the jth comparison star, k is the number of comparison stars and $\sigma_{j,i}$ is the scaled square deviation. $\sigma_{j,i}$ is given as

$$\sigma_{j,i} = s_j (m_{j,i} - \langle m_j \rangle)^2, \tag{10}$$

where $m_{j,i}$ is the magnitudes of each comparison star, $\langle m_j \rangle$ is the mean magnitude of the comparison star, and s_j is the scaling factor to account for the different SNRs of the comparison stars. s_j is given as

$$s_j = \frac{\langle \sigma^2_{\rm blazar} \rangle}{\langle \sigma^2_{sj} \rangle}, \tag{11}$$

where $\langle \sigma^2_{\rm blazar} \rangle$ and $\langle \sigma^2_{sj} \rangle$ are the average square errors of the blazar and comparison star magnitudes, respectively. Its critical value was determined at the 99.9 per cent confidence level ($\alpha = 0.001$) with the degrees of freedom for the blazars being one less than the number of observations, and the degrees of freedom for the comparison stars being the sum of one less than the number of observations for each comparison star.

Finally, the $F_{\rm enh}$ values with critical values are shown in column 7 in Table 2. They show significant detections of variability in 15/48 instances across all sources, dates, and filters. 12 of these detections correspond to observations in all filters of OJ287 on 2023 January 15, and PKS 0735+178 on 2023 January 15 and 17.

4.5 Temporal variability summary

We summarize the results of each test in Table 2 and determine epochs of variability, we look at the results of the fractional variability, χ^2, and enhanced F-test analyses and determine variable epochs if all three tests are passed. If one or fewer tests were met, we considered there to be no evidence for intranight variability in these sources/epochs. Overall all TXS 0506+056 and OJ248 epochs display no significant levels of intranight variability. There is possible variability from TXS 0506+056 on 2023 January 16. Given that this possible variability only occurs in the i band, we consider this likely a result of scatter in the data. OJ287 shows one epoch of significant variability on 2023 January 15. PKS 0735+178 shows two epochs of significant variability on 2023 January 15 and 17 and one of possible significant variability on 2023 January 16. The latter consists of very few observations due to poor observing conditions so, based on the light curve, it is possible that this is a false detection. We show the light curves with statistically significant variability for OJ287 and PKS 0735+178 in Figs 1–3 and will discuss these variable epochs further in later sections.

5 COLOUR VARIABILITY

We test for colour variability by investigating how the $g - z_s$ colour changes with respect to r-band magnitude and with time. We use the Spearman rank correlation coefficients to quantify the level of

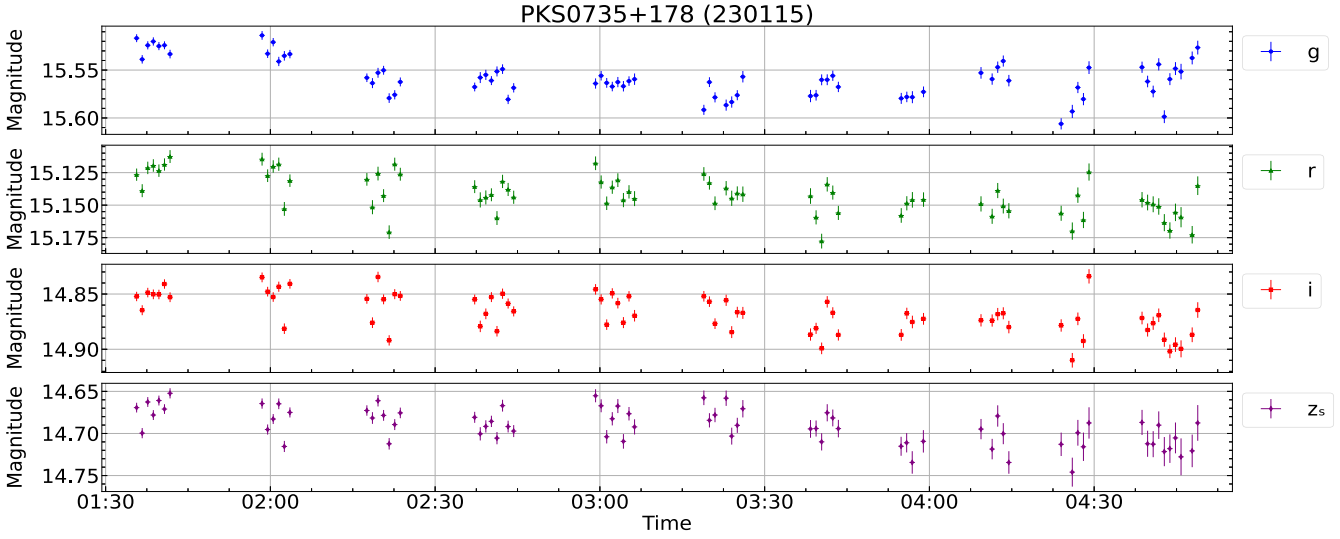

Figure 2. As Fig. 1, but for PKS 0735+178 on the night of 2023 January 15.

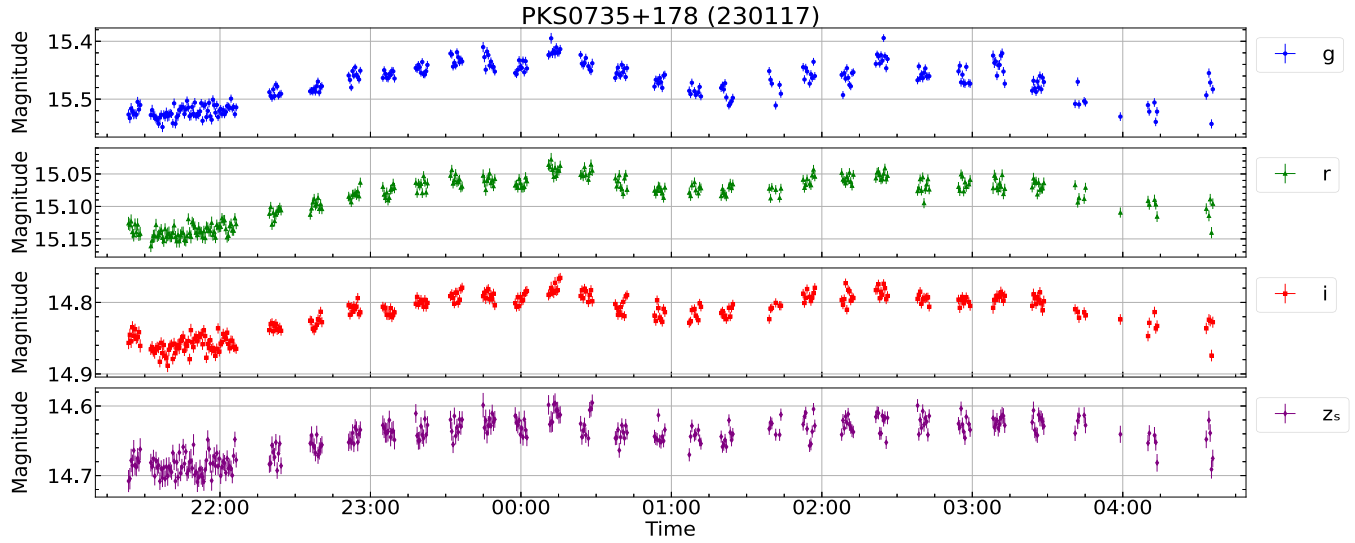

Figure 3. As Fig. 1, but for PKS 0735+178 on the night of 2023 January 17.

Table 3. Correlation strengths for Spearman rank correlation coefficients. The magnitude of c shows whether the correlation is positive or negative.

Value	Correlation degree
$c = 0$	No correlation
$0 \leq \lvert c \rvert < 0.2$	Very weak
$0.2 \leq \lvert c \rvert < 0.4$	Weak
$0.4 \leq \lvert c \rvert < 0.6$	Moderate
$0.6 \leq \lvert c \rvert < 0.8$	Strong
$0.8 \leq \lvert c \rvert < 1$	Very strong
$\lvert c \rvert = 1$	Monotonic

monotonic variability observed in each source on a given night. We use $\alpha = 0.05$ for the significance coefficient, p, implying a 95 per cent confidence interval and assign the strength of the correlation, c, by the ranges specified in Table 3. We also utilize the enhanced F-test to account for the variability of the reference stars as previously described.

Table 4. Colour variability statistics for variable sources on a given night. p and c refer to the Spearman rank correlation coefficients (significance and strength respectively), $F_{\rm enh}$ is the enhanced F-test value with the critical value as described in Section 4.4, and the final column describes whether or not the colour of the source was deemed variable on the given night. If $p < 0.05$ and $F_{\rm enh} > F_{\rm crit}$, the source was deemed variable (V), otherwise not variable (NV).

Source	Date	p	c	$F_{\rm enh}$ ($F_{\rm crit}$)	Variable?
OJ287	2023 Jan 15	0.07	−0.12	0.88 (1.53)	NV
PKS 0735+178	2023 Jan 15	4.6×10^{-3}	0.33	4.66 (1.72)	V
...	2023 Jan 16	0.7	−0.08	1.84 (2.40)	NV
...	2023 Jan 17	3.9×10^{-10}	−0.35	3.13 (1.31)	V

The Spearman rank correlation coefficients and enhanced F-test values for each set of $g - z_{\rm s}$ versus r data are shown in Table 4 (full table for all epochs available in Table B1 with the corresponding plots in Fig. B5 in Appendix B). There are two epochs that show significant colour variability during observations; PKS 0735+178 on

the nights of 2023 January 15 and 17. The former shows a positive correlation with a strength of 0.33, indicating a weak correlation. The positive nature of this correlation implies as the source gets brighter, it also gets redder in colour. Conversely, the latter date shows a negative correlation with a strength of 0.35, again indicating a weak correlation, although the negative nature this time indicates as the source gets brighter, it also gets bluer.

To confirm these results, we also obtained correlation statistics on the slope of the optical spectral energy distribution (SED) versus the *r*-band magnitude. The slope was obtained by fitting a line through the *g*-, *i*-, z_s-band magnitudes at each epoch. This analysis confirmed the same sources and epochs to show significant variability as the colour analysis (see Appendix A for details).

6 TIME-LAG ANALYSIS

We test for the possibility of a time lag between $griz_s$ bands on the nights where sources show statistically significant variability. This would be indicative of a shock or any energy density evolution within the jet, and allow us to rule out geometric variability processes like Doppler factor evolution of spiralling emitting regions. The variability must occur over time-scales less than the duration of the observations (minima and maxima within the light curves), which allows us to match up light curve features between bands and test for intraband lags. Only one source and night fit these criteria, PKS 0735+178 on 2023 January 17. To perform the lag analysis, we utilize the discrete correlation function (DCF) which provides an estimate for the time lag between two unevenly sampled time series without the need for interpolation, while accounting for the effects of correlated errors (Edelson & Krolik 1988). It is defined by

$$\mathrm{UDCF}_{ij} = \frac{(x_i - \langle x \rangle)\left(y_j - \langle y \rangle\right)}{\sqrt{\left(\sigma_x^2 - \langle \Delta x \rangle^2\right)\left(\sigma_y^2 - \langle \Delta y \rangle^2\right)}}, \tag{12}$$

where (x_i, y_j) are the observations, $(\langle x \rangle, \langle y \rangle)$ are the mean value from each light curve, (σ_x, σ_y) are the standard deviation of each light curve, and $(\langle \Delta x \rangle, \langle \Delta y \rangle)$ are the median error values (Liodakis et al. 2018). To find the DCF value associated with each time shift, τ, we average over the number of (x_i, y_j) pairs, N, where $\tau - \frac{\Delta\tau}{2} < \Delta t_{ij} < \tau + \frac{\Delta\tau}{2}$ or in this case, the mean UDCF_{ij} value

$$\mathrm{DCF}(\tau) = \frac{\sum \mathrm{UDCF}_{ij}}{N} = \langle \mathrm{UDCF}_{ij} \rangle. \tag{13}$$

What also sets the DCF apart from other correlation methods is that a standard error on $DCF(\tau)$ can be given by

$$\Delta\mathrm{DCF}(\tau) = \frac{1}{N-1}\left(\sqrt{\sum \left(\mathrm{UDCF}_{ij} - \mathrm{DCF}(\tau)\right)^2}\right), \tag{14}$$

assuming the individual UDCF_{ij} values within a bin are uncorrelated.

We investigate the possibility of a lag within ± 60 min. While analysing the data using the DCF, its limitations in accounting for regularly unevenly sampled data became apparent. The data consists of an observing sequence over ~ 5 min before a ~ 10 min break whilst observing a second target. When performing the DCF, this periodically resulted in a large decrease in the number of overlapping bins, zero in some instances, within $\frac{\Delta\tau}{2}$. This is seen in the correlation curves (Fig. 4) as periodic peaks and drops in the coefficient values.

Fig. 4 shows the results of the DCF on the data from PKS 0735+178 on the night of 2023 January 17 on each $griz_s$ light curve with respect to the *g* light curve. In this configuration, a positive lag implies *g* leading the other bands and a negative lag implies *g* lagging the other bands. The solid curve shows a Gaussian fit to the DCF correlation values, calculated to offset the structure induced by the periodic number of overlapping bins. The dotted line shows the peak of the Gaussian curve, and therefore the lag value. It shows a significant non-zero lag in each riz_s light curve with respect to *g*. Between the three bands, the lags are all consistent, with a mean value of -6.94 ± 1.43 min. The uncertainty of 1.43 min is the average cadence of the observations and was chosen as the larger value of average cadence and error on the Gaussian peak.

In order to check the significance of the induced correlation curve structure, and to mitigate the scatter in the light curves, we also calculated the DCF after fitting a curve to the data. We fit each light curve using the GaussianProcessRegressor module from scikit-learn in Python (Pedregosa et al. 2011) using the Rational Quadratic kernel. Calculating the DCF on this fitted curve and following the same steps as outlined previously, we obtain the results shown in Fig. 5. We keep the same uncertainties (1.43 min) to reflect the original data cadence. The results for *g* and *i* are consistent with the values obtained previously, but the lags obtained in *r* and z_s are significantly larger at -11.68 ± 1.43 min and -15.48 ± 1.43 min, respectively.

7 DISCUSSION

Blazar intranight variability is thought to arise from geometric changes within the blazar jet; such as the Doppler factor variability of an emitting region travelling in a helical motion in the jet, from the evolution of an emitting region through the jet or from the acceleration/cooling of particles. Additionally, it is entirely possible for the observed behaviour to be a combination of multiple emitting regions or different processes occurring simultaneously.

The mechanism behind Doppler factor variability involves an emitting region, or 'blob', of density inhomogeneity travelling helically along the jet. This causes quasi-periodic oscillations (QPOs) in the light curve resulting from the apparent changing Doppler factor and subsequent bulk Lorentz factor (Camenzind & Krockenberger 1992; Mohan & Mangalam 2015; Bachev et al. 2023). On intranight time-scales, this behaviour would present across the optical regime as multiple brightness peaks, depending on the number of blobs, where individual peaks would be observed with no colour changes or time lags (Papadakis et al. 2004; Bachev 2015). If the origin of the variability was many emitting blobs, each with differing SEDs, then one might expect the emission of different blobs to dominate at different times and subsequently cause rapid colour changes in addition to the brightness changes (Bachev et al. 2023). This variability, however, is a relativistic effect rather than any change in the emission output of the source.

Changes in the intrinsic luminosity of the source on intranight time-scales can be attributed to processes such as shocks or magnetic reconnection in the jet. These processes involve a uniform injection of fresh, more energetic electrons which evolve as a function of their energy distribution, where harder electrons cool faster (Urry et al. 1997). This may produce intra- and inter-band time lags, which can determine cooling times and constrain the homogeneous synchrotron model (Tavecchio, Maraschi & Ghisellini 1998). An evolving energy distribution may also produce colour variability (Papadakis et al. 2004). Additionally, emission at optical frequencies can trace slightly different parts of the SED depending on the location of the synchrotron peak. For LSP sources (three of our sources), optical frequencies trace the falling region of the synchrotron peak which means redder frequencies map higher-energy emission and may produce faster-evolving variability, causing colour variability and time lags between wavebands. Conversely, for HSP blazars,

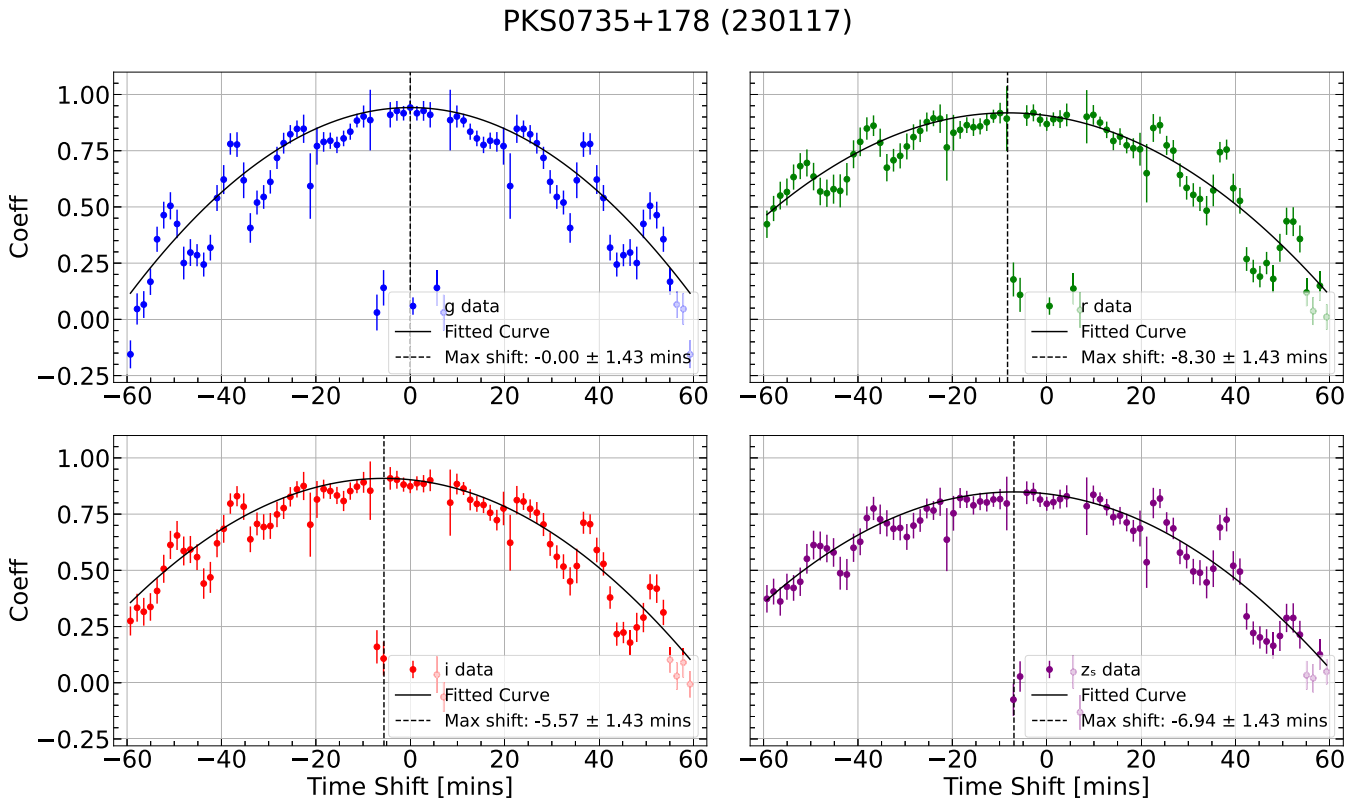

Figure 4. DCF coefficients testing for a lag on the data from PKS 0735+178 on the night of 2023 January 17. The coefficients are fitted with a Gaussian (solid line) to find the peak. This peak value (vertical dotted line) is shown in the legend with an uncertainty.

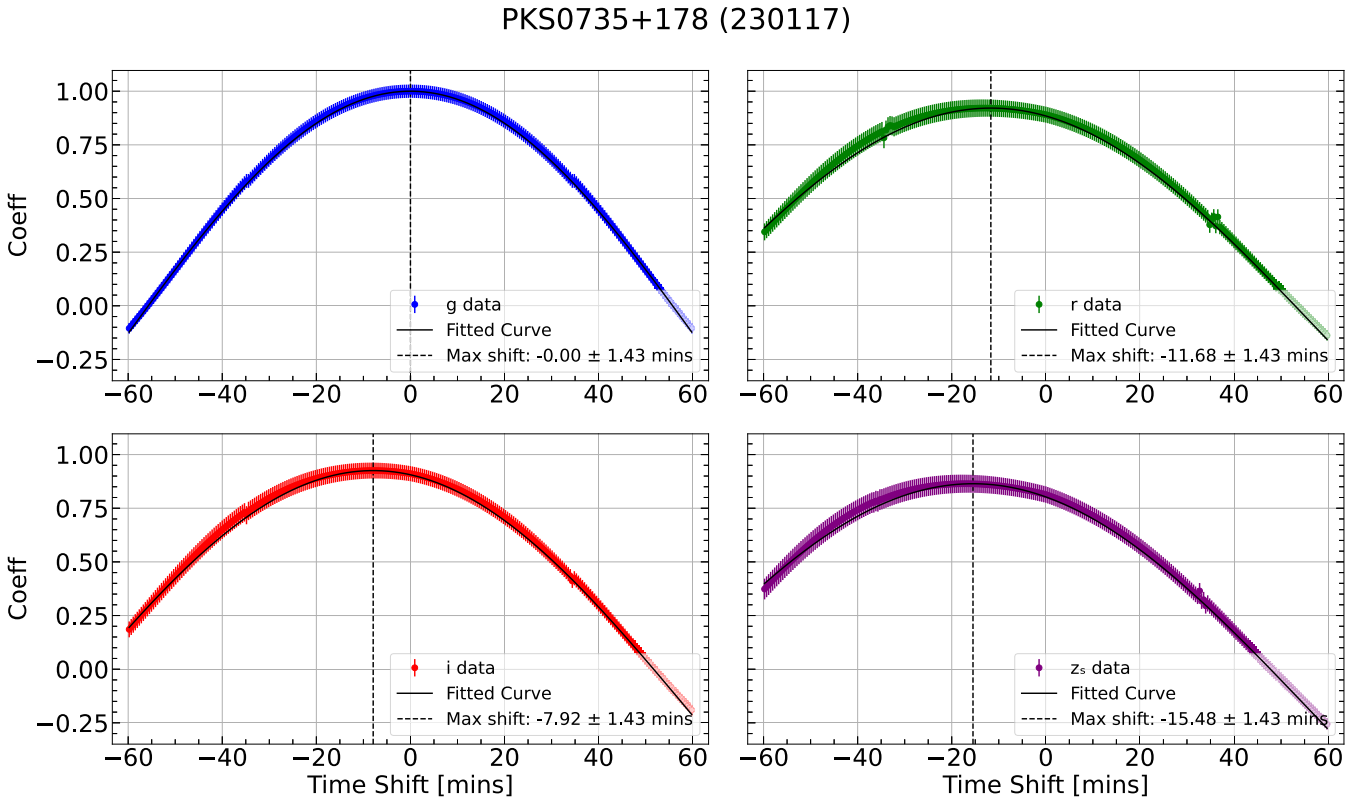

Figure 5. As Fig. 4, but with the fitted data from PKS 0735+178 on the night of 2023 January 17.

optical frequencies trace the rising part of the SED so one would expect the bluer frequencies to evolve faster (Subbu Ulaganatha Pandian et al. 2022).

In our work, we found that TXS 0506+056 and OJ248 showed no evidence of variability in the epochs studied. OJ248 is the faintest object in our sample and would have benefitted from longer exposure times for better signal-to-noise had the autoguider on the TCS been available. TXS 0506+056 showed significant, weak, colour variability on 2023 January 15, which may be due to the scatter in the data.

OJ287 showed evidence of significant flux variability on the night of 2023 January 15, but no significant changes in colour. There are no significant short-time-scale features in the light curve, and the observed variability consists of a gradual decrease in the brightness over the $\sim$ 6 hours of observing.

PKS 0735+178 displayed significant variability on two out of three nights, including significant colour correlations showing both redder-when-brighter and bluer-when-brighter behaviour. Additionally, on the night when BWB colour variability was observed, a hard lag of order 10 min was detected.

If the hard lags observed in PKS 0735+178 are caused by the evolution of the electron energy distribution, different shock-in-jet processes can be examined to explain the variability. When the acceleration time-scale during the shock is much less than the post-shock cooling time-scale, i.e. $t_{\rm acc} \ll t_{\rm cool}$, soft lags are expected, where the lower energy emission (red) lag behind the higher energy emission (blue). Conversely, when the acceleration time-scale is comparable to the cooling time-scale, i.e. $t_{\rm acc} \approx t_{\rm cool}$, hard lags are expected, where the lower energy emission precedes the higher energy emission (Zhang et al. 2002).

In order to achieve a hard lag, and produce comparable acceleration and cooling time-scales, an energy injection is required to accelerate electrons after the shock has passed, rather than allowing the shocked particles to cool, which results in soft lags (Mastichiadis & Moraitis 2008). Injecting energy into the post-shocked medium can be achieved using second-order Fermi acceleration processes. Kalita et al. (2023) describe how turbulent magnetic fields built behind a shock travelling through an inhomogeneous medium can produce these processes, resulting in acceleration of the post-shock particles via magnetic reconnection. In this scenario, energy is released to the surrounding particles through the interaction of magnetic field lines with opposite polarity.

While we cannot make a firm conclusion as to the nature of the detected INOV in PKS 0735+178, the detection of a hard lag favours changes to the electron energy distributions and the internal shock model over any geometric changes.

8 CONCLUSION

We performed simultaneous g, r, i, $z_{\rm s}$ photometric observations using MuSCAT2 on the Carlos Sánchez Telescope to study the intranight optical variability of four γ-ray bright blazars. Our analysis consisted of employing several statistical methods to test for the presence of variability on time-scales of a few hours. Additionally, the DCF was used to test for intra-band time lags between bands r, i, and $z_{\rm s}$ with respect to band g. We found:

(i) TXS 0506+056 and OJ248 showed no evidence for intranight variability on any night.

(ii) OJ287 showed evidence for intranight variability on 2023 January 15. The nature of this variability was a gradual change, around 0.1 magnitudes over 7 hours, and was not accompanied by any significant changes in colour.

(iii) PKS 0735+178 showed evidence for intranight variability on two occasions along with changes in colour; showing both an RWB and a BWB correlation on different dates.

(iv) PKS 0735+178 showed a time lag where the g band lags the r, i, $z_{\rm s}$ bands by around 10 min. This suggests the variability may arise from changes in the electron energy-density distribution.

Further observations of blazars during all activity states at high cadences can confirm whether intraband hard lags across optical frequencies are a more common feature than previously thought. This would provide strong evidence for changes in the jet's energy density as the cause for INOV in blazars.

ACKNOWLEDGEMENTS

We would like to thank the reviewer for their constructive comments. This article is based on observations made with the Carlos Sanchez Telescope operated on the island of Tenerife by the Instituto de Astrofiscia de Canarias in the Spanish Observatorio del Teide. The Liverpool Telescope is operated on the island of La Palma by Liverpool John Moores University in the Spanish Observatorio del Roque de los Muchachos of the Instituto de Astrofisica de Canarias with financial support from the UKRI Science and Technology Facilities Council (STFC) (ST/T00147X/1). HEJ acknowledges travel support from the UKRI STFC PATT grant (ST/S001530/1).

DATA AVAILABILITY

The data underlying this article will be shared on reasonable request to the corresponding author.

REFERENCES

Abdo A. A. et al., 2010, ApJ, 716, 30
Abdollahi S. et al., 2023, ApJS, 265, 31
Abdurro'uf et al., 2022, ApJS, 259, 35
Acciari V. A. et al., 2022, ApJ, 927, 197
Bachev R., 2015, MNRAS, 451, L21
Bachev R., Semkov E., Strigachev A., Gupta A. C., Gaur H., Mihov B., Boeva S., Slavcheva-Mihova L., 2012, MNRAS, 424, 2625
Bachev R., Strigachev A., Kurtenkov A., Spassov B., Nikolov Y., Boeva S., Semkov E., 2021, Bulg. Astron. J., 34, 79
Bachev R. et al., 2023, MNRAS, 522, 3018
Bhatta G. et al., 2015, ApJ, 809, L27
Böttcher M., Dermer C. D., 2010, ApJ, 711, 445
Böttcher M., Reimer A., Sweeney K., Prakash A., 2013, ApJ, 768, 54
Camenzind M., Krockenberger M., 1992, A&A, 255, 59
Carnerero M. I. et al., 2015, MNRAS, 450, 2677
Carswell R. F., Strittmatter P. A., Williams R. E., Kinman T. D., Serkowski K., 1974, ApJ, 190, L101
Chand K. G.-K., Omar A., Chand H., Mishra S., Bisht P. S., Britzen S., 2021, MNRAS, 511, L13
Chatterjee R. et al., 2008, ApJ, 689, 79
D'Ammando F., Orienti M., 2012, Astron. Telegram, 4440, 1
Dermer C. D., Schlickeiser R., 1993, ApJ, 416, 458
de Diego J. A., 2014, AJ, 148, 93
Dzhilkibaev Z. A., Suvorova O., Baikal-GVD Collaboration, 2021, Astron. Telegram, 15112, 1
Edelson R. A., Krolik J. H., 1988, ApJ, 333, 646
Edelson R., Turner T. J., Pounds K., Vaughan S., Markowitz A., Marshall H., Dobbie P., Warwick R., 2002, ApJ, 568, 610
Falomo R., Treves A., Paiano S., 2021, Astron. Telegram, 15132, 1

Fan J.-H., Bastieri D., Yang J.-H., Liu Y., Hua T.-X., Yuan Y.-H., Wu D.-X., 2014, Res. Astron. Astrophys., 14, 1135
Filippini F. et al., 2022, Astron. Telegram, 15290, 1
Fiorucci M., Ciprini S., Tosti G., 2004, A&A, 419, 25
Flewelling H. A. et al., 2020, ApJS, 251, 7
Fossati G., Maraschi L., Celotti A., Comastri A., Ghisellini G., 1998, MNRAS, 299, 433
Garrappa S., Buson S., Sinapius J., Kadl M., 2021, Astron. Telegram, 15099, 1
Gaur H., 2014, JA&A, 35, 241
Gaur H., Gupta A. C., Wiita P. J., 2012, AJ, 143, 23
Ghisellini G., Celotti A., Fossati G., Maraschi L., Comastri A., 1998, MNRAS, 301, 451
Ghisellini G., Tavecchio F., Foschini L., Sbarrato T., Ghirlanda G., Maraschi L., 2012, MNRAS, 425, 1371
Gopal-Krishna, Wiita P. J., 1992, A&A, 259, 109
Gu M. F., Lee C. U., Pak S., Yim H. S., Fletcher A. B., 2006, A&A, 450, 39
Heidt J., Wagner S. J., 1996, A&A, 305, 42
Henden A. A., Levine S., Terrell D., Welch D. L., Munari U., Kloppenborg B. K., 2018, AAS Meeting, 232, p. 223.06
Hovatta T., Valtaoja E., Tornikoski M., Lähteenmäki A., 2009, A&A, 494, 527
IceCube Collaboration, 2021, GCN Circ., 31191, 1
IceCub Collaboration et al., 2018, Science, 361, eaat1378
Jorstad S. G. et al., 2022, Nature, 609, 265
Kadler M. et al., 2021, Astron. Telegram, 15105, 1
Kalita N. et al., 2023, ApJ, 943, 135
Katz J. I., 1997, ApJ, 478, 527
Keivani A. et al., 2018, ApJ, 864, 84
Kirk J. G., Rieger F. M., Mastichiadis A., 1998, A&A, 333, 452
Kopper C., Blaufuss E., 2017, GRB Coordinates Network, 21916, 1
Lang D., Hogg D. W., Mierle K., Blanton M., Roweis S., 2010, AJ, 139, 1782
Lewis T. R., Karwin C. M., Venters T. M., Fleischhack H., Sheng Y., Kierans C. A., Caputo R., McEnery J., 2021, preprint (arXiv:2111.10600)
Liodakis I., Romani R. W., Filippenko A. V., Kiehlmann S., Max-Moerbeck W., Readhead A. C. S., Zheng W., 2018, MNRAS, 480, 5517
Maraschi L., Ghisellini G., Celotti A., 1992, ApJ, 397, L5
Massaro E., Maselli A., Leto C., Marchegiani P., Perri M., Giommi P., Piranomonte S., 2015, Ap&SS, 357, 75
Mastichiadis A., Moraitis K., 2008, A&A, 491, L37
Miller H. R., Carini M. T., Goodrich B. D., 1989, Nature, 337, 627
Mohan P., Mangalam A., 2015, ApJ, 805, 91
Narita N. et al., 2019, J. Astron. Tel. Instr. Syst., 5, 015001
Negi V., Joshi R., Chand K., Chand H., Wiita P., Ho L. C., Singh R. S., 2022, MNRAS, 510, 1791
Nilsson K., Pursimo T., Villforth C., Lindfors E., Takalo L. O., Sillanpää A., 2012, A&A, 547, A1
Nilsson K. et al., 2018, A&A, 620, A185
Olguín-Iglesias A. et al., 2016, MNRAS, 460, 3202
Orienti M., D'Ammando F., 2012, Astron. Telegram, 4421, 1
Osorio M., Rangel E., Sacahui J. R., González M. M., 2023, Astron. Nachr., 344, e20230084
Paczynski B., 1996, ARA&A, 34, 419
Padovani P., Oikonomou F., Petropoulou M., Giommi P., Resconi E., 2019, MNRAS, 484, L104
Paiano S., Falomo R., Treves A., Scarpa R., 2018, ApJ, 854, L32
Papadakis I. E., Samaritakis V., Boumis P., Papamastorakis J., 2004, A&A, 426, 437
Pedregosa F. et al., 2011, J. Mach. Learn. Res., 12, 2825
Petkov V. B., Novoseltsev Y. F., Novoseltseva R. V., Baksan Underground Scintillation Telescope Group, 2021, Astron. Telegram, 15143, 1
Poutanen J., Zdziarski A. A., Ibragimov A., 2008, MNRAS, 389, 1427
Prandini E., Ghisellini G., 2022, Galaxies, 10, 35
Rajagopal M., Marcotulli L., Ajello M., Kaur A., Paliya V., Hartmann D., 2020, ApJ, 889, 102
Rodrigues X., Gao S., Fedynitch A., Palladino A., Winter W., 2019, ApJ, 874, L29
Romero G. E., Cellone S. A., Combi J. A., 1999, A&AS, 135, 477
Sagar R., Stalin C. S., Gopal-Krishna, Wiita P. J., 2004, MNRAS, 348, 176
Sahakyan N., Giommi P., Padovani P., Petropoulou M., Bégué D., Boccardi B., Gasparyan S., 2023, MNRAS, 519, 1396
Santander M., Buson S., 2021, Astron. Telegram, 15102, 1
Schleicher B. et al., 2019, Galaxies, 7,62
Shrestha M., Steele I. A., Piascik A. S., Jermak H., Smith R. J., Copperwheat C. M., 2020, MNRAS, 494, 4676
Sillanpaa A., Haarala S., Valtonen M. J., Sundelius B., Byrd G. G., 1988, ApJ, 325, 628
Sillanpaa A. et al., 1996, A&A, 305, L17
Singh K. K. et al., 2018, Astropart. Phys., 103, 122
Sitko M. L., Junkkarinen V. T., 1985, PASP, 97, 1158
Smith R. J., Piascik A. S., Steele I. A., Barnsley R. M., 2016, SPIE, 9913, 17
Stickel M., Padovani P., Urry C. M., Fried J. W., Kuehr H., 1991, ApJ, 374, 431
Stickel M., Fried J. W., Kuehr H., 1993, A&AS, 98, 393
Pandian K. S. U., Natarajan A., Stalin C. S., Pandey A., Muneer S., Natarajan B., 2022, JA&A, 43, 48
Sundelius B., Wahde M., Lehto H. J., Valtonen M. J., 1997, ApJ, 484, 180
Tanaka Y. T., Buson S., Kocevski D., 2017, Astron. Telegram, 10791, 1
Tavecchio F., Maraschi L., Ghisellini G., 1998, ApJ, 509, 608
Urry C. M., 1998, Adv. Space Res., 21, 89
Urry C. M., Padovani P., 1995, PASP, 107, 803
Urry C. M. et al., 1997, ApJ, 486, 799
Valtonen M. J. et al., 2006, ApJ, 646, 36
Vaughan S., Edelson R., Warwick R. S., Uttley P., 2003, MNRAS, 345, 1271
Wu J., Zhou X., Ma J., Wu Z., Jiang Z., 2009, in Wang W., Yang Z., Luo Z., Chen Z., eds, ASP Conf. Ser. Vol. 408, The Starburst-AGN Connection. Astron. Soc. Pac., San Francisco, p. 278
Zeng W. et al., 2017, Galaxies, 5, 85
Zhang Y. H. et al., 2002, ApJ, 572, 762
Zhang B.-K., Zhou X.-S., Zhao X.-Y., Dai B.-Z., 2015, Res. Astron. Astrophys., 15, 1784
Zhirkov K. et al., 2021, Astron. Telegram, 15098, 1

APPENDIX A: SPECTRAL INDEX

We study the change in SED of each source on a given night by calculating the gradient of a straight line fitted through the *g*-, *i*-, and z_z-band magnitudes at each epoch, and correlating it against the corresponding *r*-band magnitude. These plots are shown in Fig. A1 where Spearman rank correlation coefficients and significance values are given above each plot. The results align very closely with what is seen in the colour–magnitude diagrams in Fig. B5, showing the same significance values for each source with very similar correlation strengths.

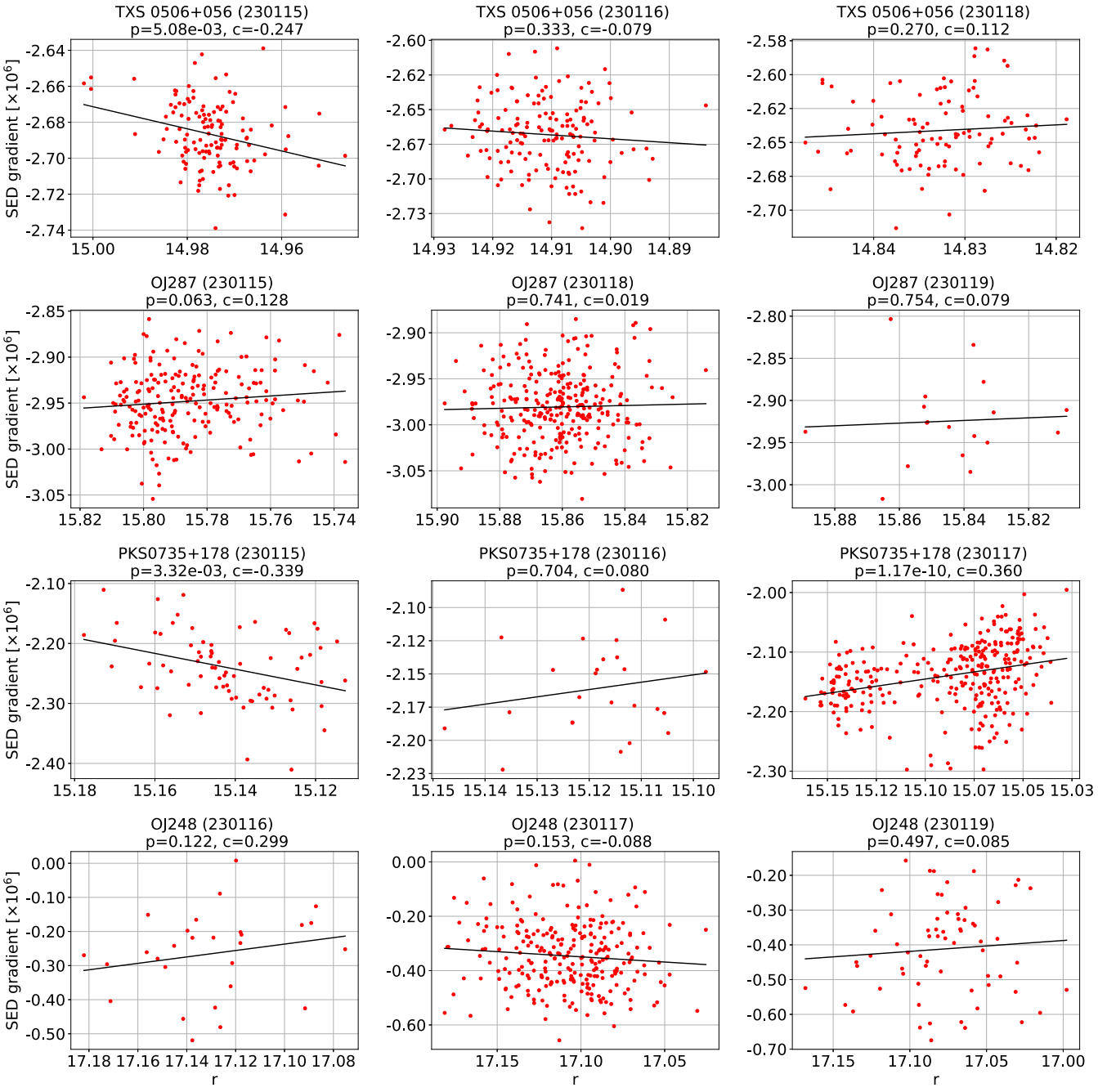

Figure A1. SED gradient using *g*-, *i*-, and z_z-band magnitudes against *r*-band magnitude for each of the four blazars (different rows) on different nights (different columns) as indicated above each plot. Spearman rank correlation coefficients and significance values are also shown above each plot.

APPENDIX B: FIGURES AND TABLES

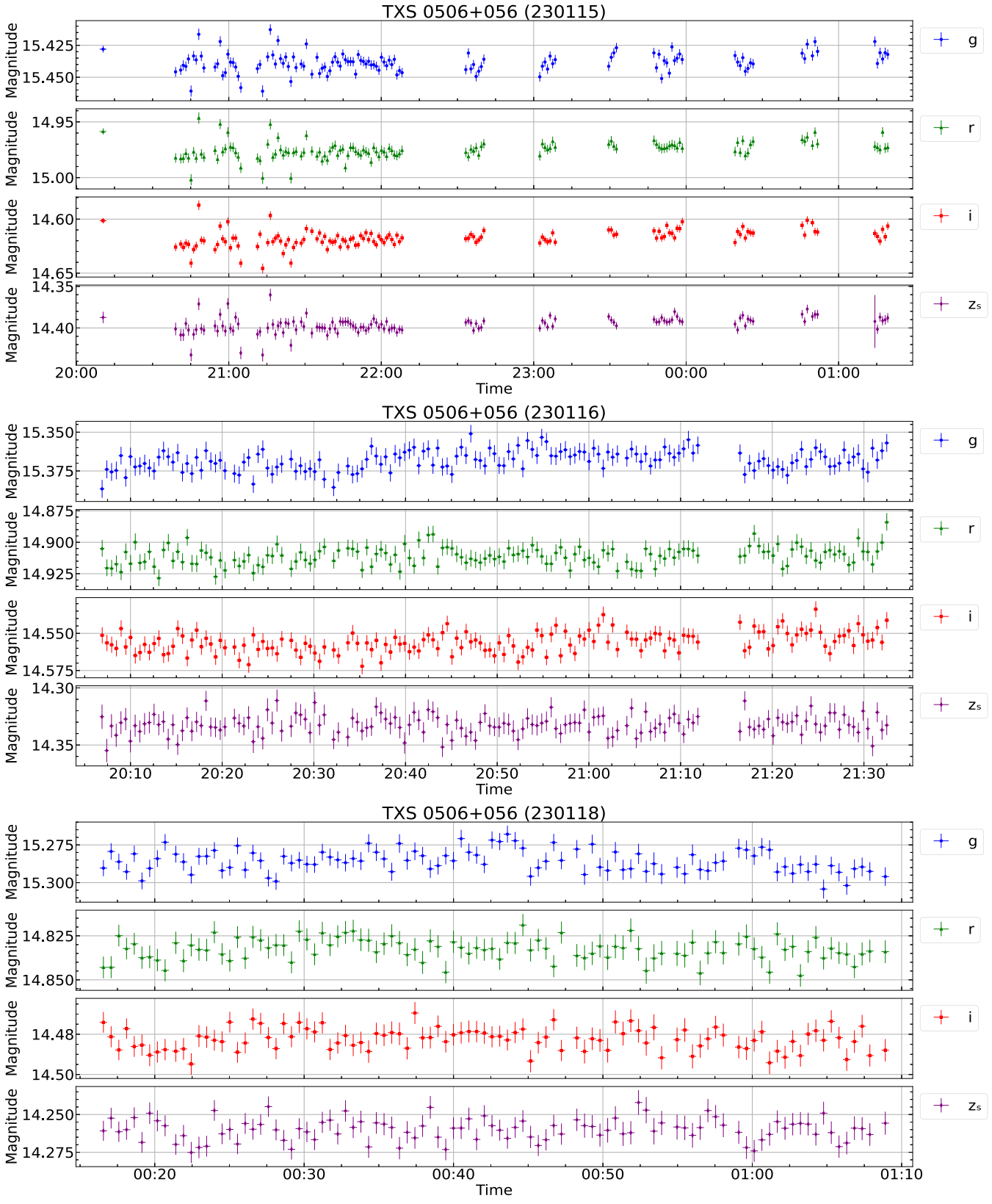

Figure B1. Light curves of TXS 0506+056 on the nights of 2023 January 15, 2023 January 16, and 2023 January 18. The panels of each of the three plots correspond to g, r, i, and z_s filters, from top to bottom. Time is given in UTC.

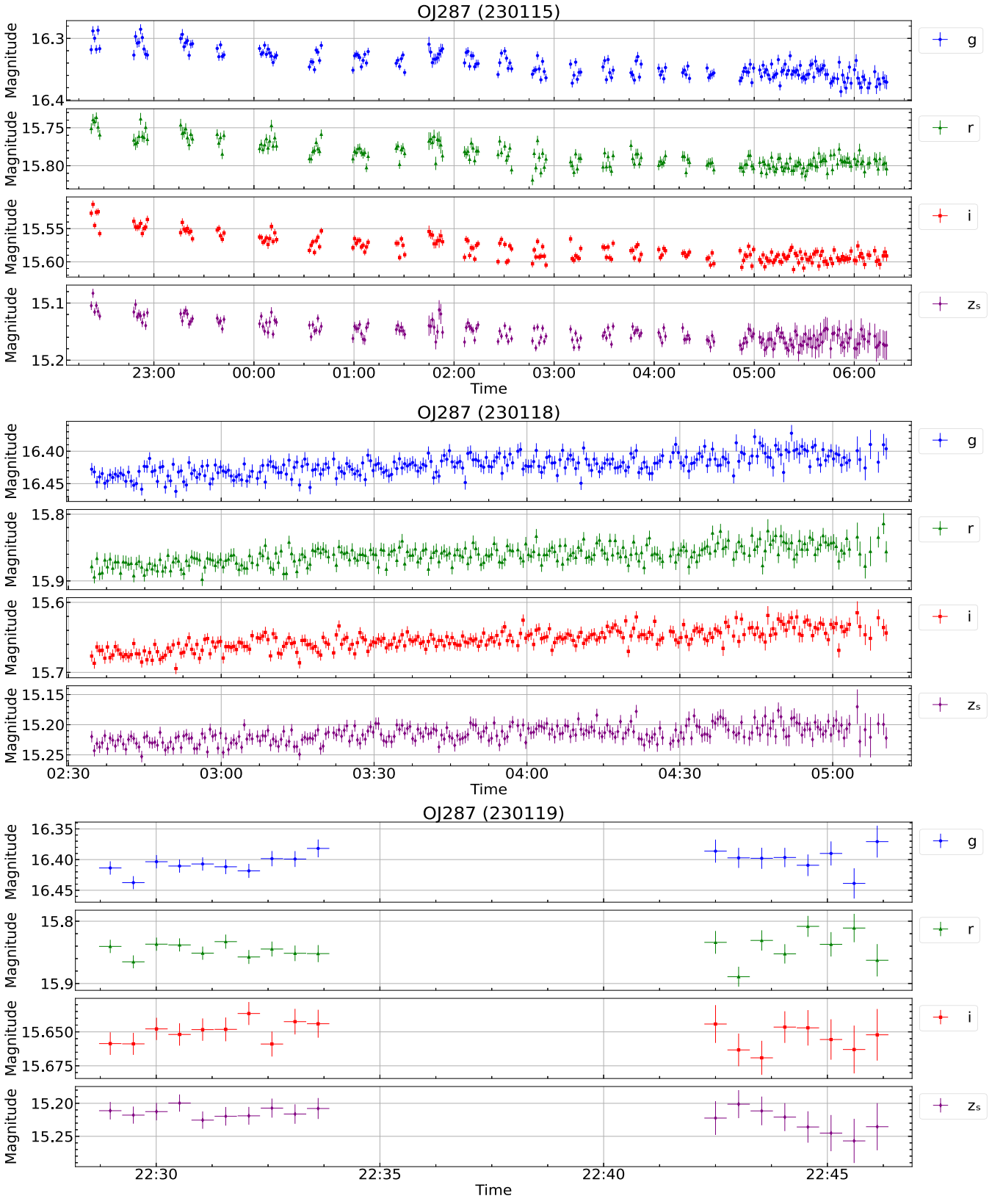

Figure B2. As Fig. B1, but for OJ287 on the nights of 2023 January 15, 2023 January 18, and 2023 January 19.

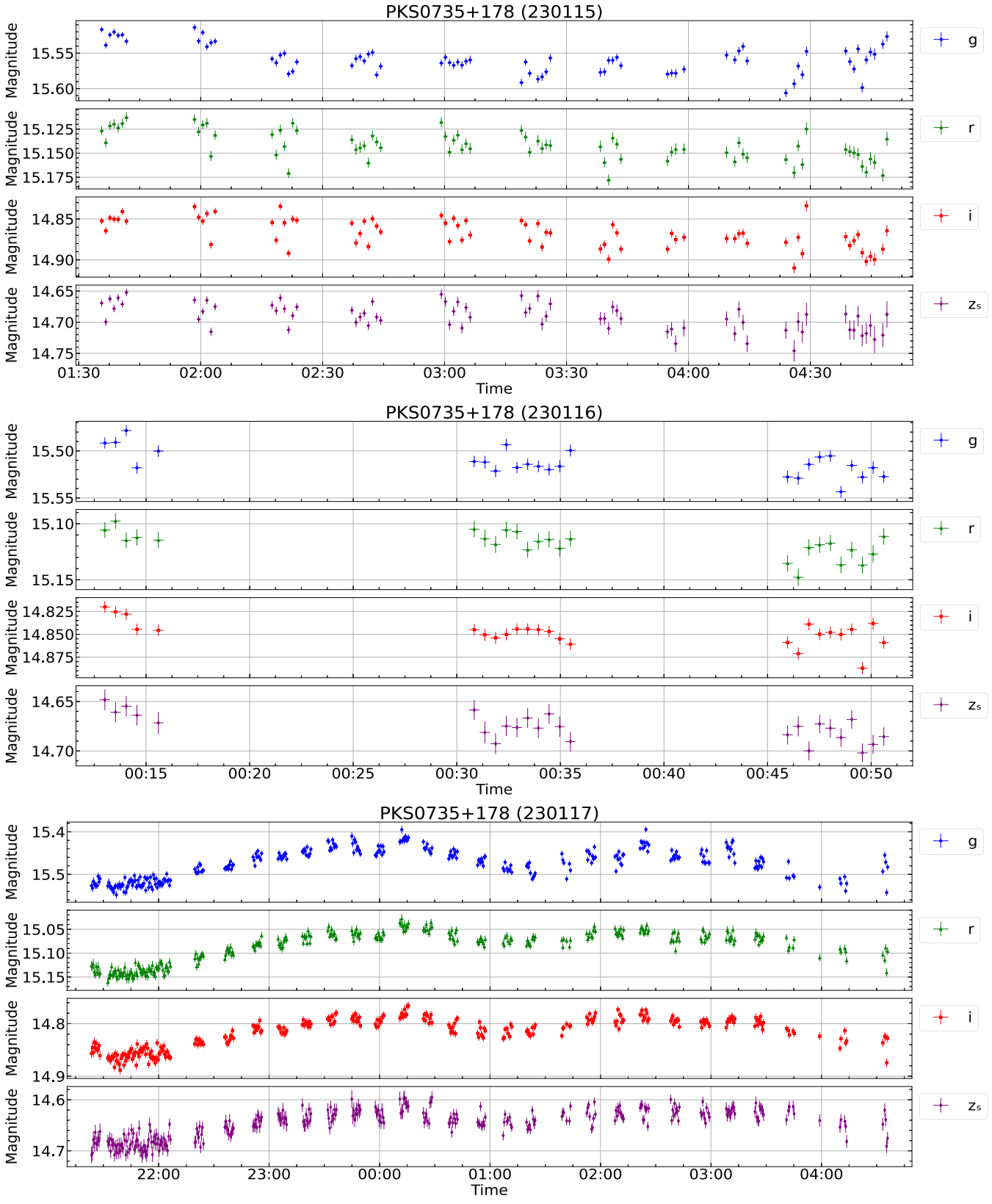

Figure B3. As Fig. B1, but for PKS 0735+178 on the nights of 2023 January 15, 2023 January 16, and 2023 January 17.

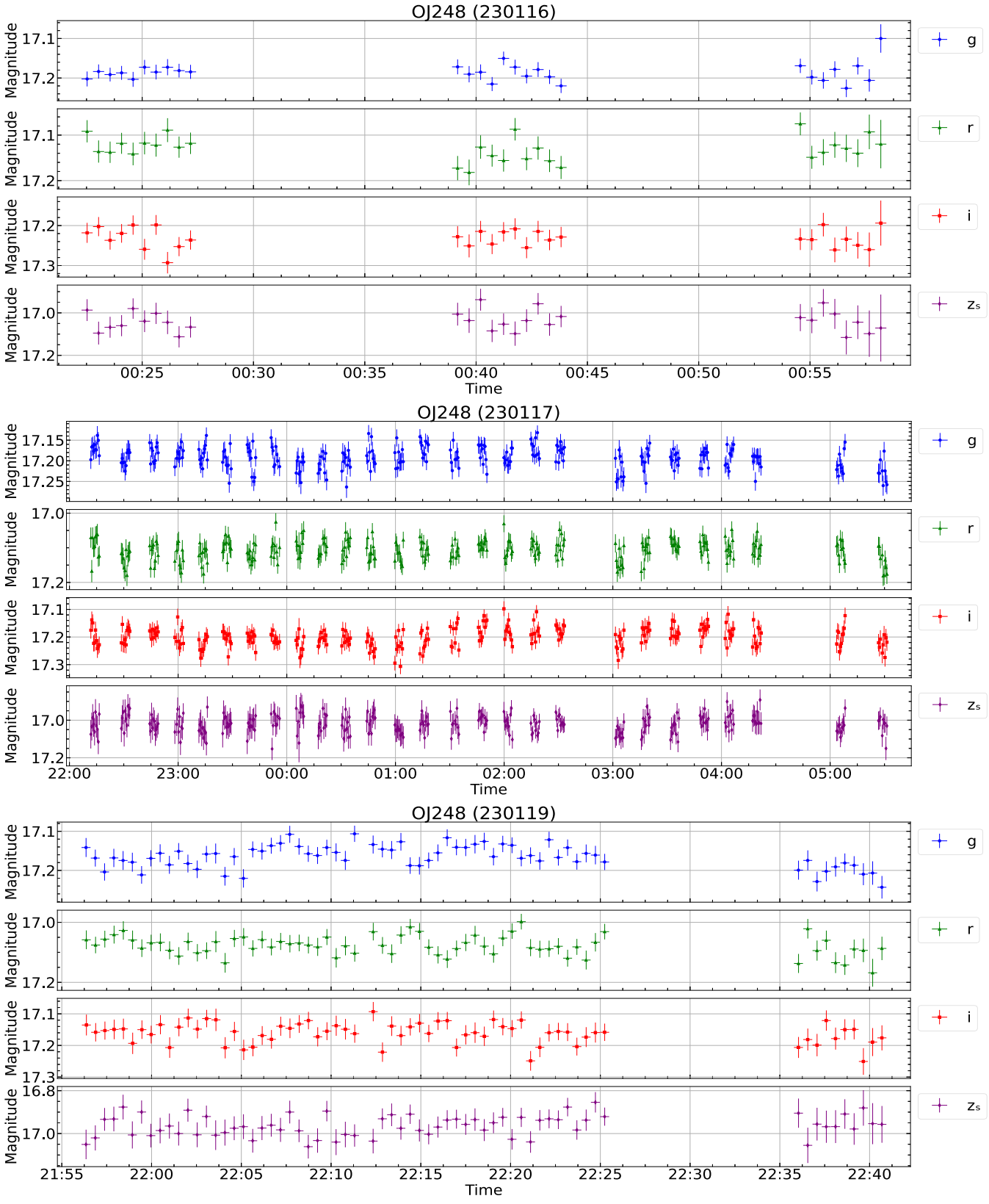

Figure B4. As Fig. B1, but for OJ248 on the nights of 2023 January 16, 2023 January 17, and 2023 January 19.

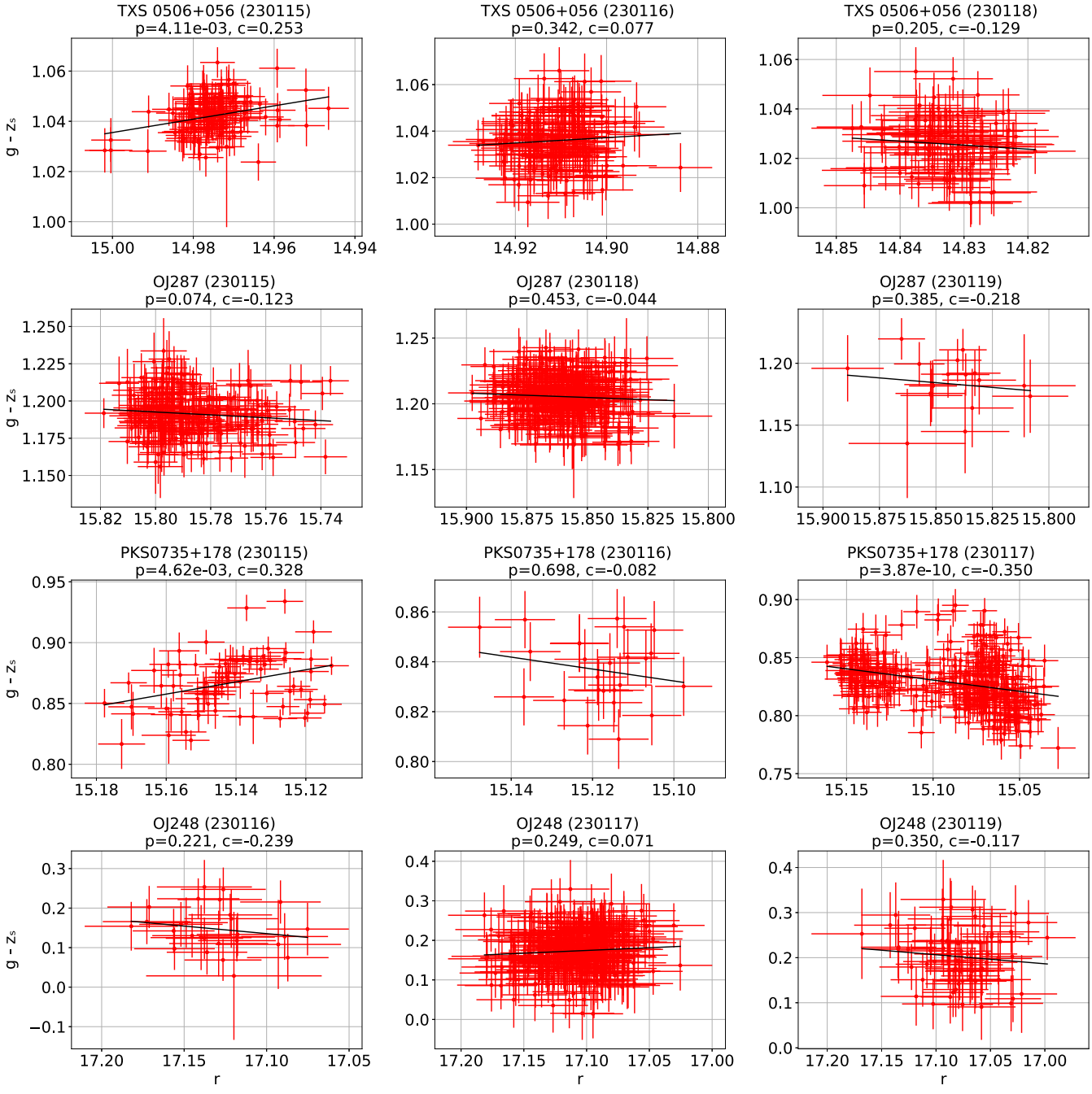

Figure B5. Colour–magnitude (r versus $g - z_s$ magnitudes) diagrams for each of the four blazars (different rows) on different nights (different columns) as indicated above each plot. Also present above each plot are the corresponding Spearman rank correlation coefficients and significance values.

Table B1. Colour variability statistics for each source on a given night. p and c refer to the Spearman rank correlation coefficients (significance and strength, respectively), $F_{\rm enh}$ is the enhanced F-test value with the critical value as described in Section 4.4, and the final column describes whether or not the colour of the source was deemed variable on the given night. If $p < 0.05$ and $F_{\rm enh} > F_{\rm crit}$, the source was deemed variable (V), otherwise not variable (NV).

Source	Date	p	c	$F_{\rm enh}$ ($F_{\rm crit}$)	Variable?
TXS 0506+056	2023 Jan 15	4.1×10^{-3}	0.25	1.11 (1.50)	NV
...	2023 Jan 16	0.34	0.08	1.41 (1.45)	NV
...	2023 Jan 18	0.21	−0.13	1.43 (1.58)	NV
OJ287	2023 Jan 15	0.07	−0.12	0.88 (1.53)	NV
...	2023 Jan 18	0.45	−0.04	0.78 (1.31)	NV
...	2023 Jan 19	0.39	−0.22	0.70 (2.79)	NV
PKS 0735+178	2023 Jan 15	4.6×10^{-3}	0.33	4.66 (1.72)	V
...	2023 Jan 16	0.7	−0.08	1.84 (2.40)	NV
...	2023 Jan 17	3.9×10^{-10}	−0.35	3.13 (1.31)	V
OJ248	2023 Jan 16	0.22	−0.24	0.41 (2.29)	NV
...	2023 Jan 17	0.25	0.07	1.15 (1.47)	NV
...	2023 Jan 19	0.35	−0.12	0.69 (1.90)	NV

This paper has been typeset from a TEX/LATEX file prepared by the author.